

# Compartment-resolved imaging of cortical functional hyperemia with OCT angiography

Harsha Radhakrishnan<sup>1,2</sup> and Vivek J. Srinivasan<sup>1,\*</sup>

<sup>1</sup>Biomedical Engineering Department, University of California Davis, Davis, CA 95616, USA

<sup>2</sup>Athinoula A. Martinos Center for Biomedical Imaging, Department of Radiology, Massachusetts General Hospital/Harvard Medical School, Charlestown, MA 02129, USA

\*vjsriniv@ucdavis.edu

**Abstract:** Optical Coherence Tomography (OCT) angiography was applied to image functional hyperemia in different vascular compartments in the rat somatosensory cortex. Dynamic backscattering changes, indicative of changes in dynamic red blood cell (dRBC) content, were used to monitor the hemodynamic response. Three-dimensional movies depicting the microvascular response to neuronal activation were created for the first time. An increase in the attenuation coefficient during activation was identified, and a simple normalization procedure was proposed to correct for it. This procedure was applied to determine compartment-resolved backscattering changes caused by dRBC content changes during functional activation. Increases in dRBC content were observed in all vascular compartments (arterial, arteriolar, capillary, and venular), with the largest responses found in the arterial and arteriolar compartments. dRBC content increased with dilation in arteries but with barely detectable dilation in veins. dRBC content increased in capillaries without significant “all or none” capillary recruitment.

©2013 Optical Society of America

**OCIS codes:** (110.4500) Optical coherence tomography; (170.3880) Medical and biological imaging; (290.1350) Backscattering; (170.1470) Blood or tissue constituent monitoring; (170.0180) Microscopy; (170.6900) Three-dimensional microscopy.

## References and links

1. K. K. Kwong, J. W. Belliveau, D. A. Chesler, I. E. Goldberg, R. M. Weisskoff, B. P. Poncelet, D. N. Kennedy, B. E. Hoppel, M. S. Cohen, R. Turner, H.-M. Cheng, T. J. Brady, and B. R. Rosen, “Dynamic magnetic resonance imaging of human brain activity during primary sensory stimulation,” *Proc. Natl. Acad. Sci. U.S.A.* **89**(12), 5675–5679 (1992).
2. S. Ogawa, D. W. Tank, R. Menon, J. M. Ellermann, S.-G. Kim, H. Merkle, and K. Ugurbil, “Intrinsic signal changes accompanying sensory stimulation: functional brain mapping with magnetic resonance imaging,” *Proc. Natl. Acad. Sci. U.S.A.* **89**(13), 5951–5955 (1992).
3. J. B. Mandeville, J. J. Marota, C. Ayata, M. A. Moskowitz, R. M. Weisskoff, and B. R. Rosen, “MRI measurement of the temporal evolution of relative CMRO<sub>2</sub> during rat forepaw stimulation,” *Magn. Reson. Med.* **42**(5), 944–951 (1999).
4. C. Martin, Y. Zheng, N. R. Sibson, J. E. Mayhew, and J. Berwick, “Complex spatiotemporal haemodynamic response following sensory stimulation in the awake rat,” *Neuroimage* **66**, 1–8 (2013).
5. M. A. Franceschini, H. Radhakrishnan, K. Thakur, W. Wu, S. Ruvinskaya, S. Carp, and D. A. Boas, “The effect of different anesthetics on neurovascular coupling,” *Neuroimage* **51**(4), 1367–1377 (2010).
6. J. P. Culver, T. Durduran, C. Cheung, A. G. Yodh, D. Furuya, and J. H. Greenberg, “Diffuse optical measurement of hemoglobin and cerebral blood flow in rat brain during hypercapnia, hypoxia and cardiac arrest,” *Adv. Exp. Med. Biol.* **510**, 293–297 (2003).
7. A. K. Dunn, “Laser speckle contrast imaging of cerebral blood flow,” *Ann. Biomed. Eng.* **40**(2), 367–377 (2012).
8. E. M. Hillman and S. A. Burgess, “Sub-millimeter resolution 3D optical imaging of living tissue using laminar optical tomography,” *Laser Photon Rev* **3**(1-2), 159–179 (2009).
9. A. Y. Shih, J. D. Driscoll, P. J. Drew, N. Nishimura, C. B. Schaffer, and D. Kleinfeld, “Two-photon microscopy as a tool to study blood flow and neurovascular coupling in the rodent brain,” *J. Cereb. Blood Flow Metab.* **32**(7), 1277–1309 (2012).
10. D. Huang, E. A. Swanson, C. P. Lin, J. S. Schuman, W. G. Stinson, W. Chang, M. R. Hee, T. Flotte, K. Gregory, C. A. Puliafito, and J. G. Fujimoto, “Optical coherence tomography,” *Science* **254**(5035), 1178–1181 (1991).

11. E. Macé, G. Montaldo, I. Cohen, M. Baulac, M. Fink, and M. Tanter, "Functional ultrasound imaging of the brain," *Nat. Methods* **8**(8), 662–664 (2011).
12. J. Fingler, D. Schwartz, C. Yang, and S. E. Fraser, "Mobility and transverse flow visualization using phase variance contrast with spectral domain optical coherence tomography," *Opt. Express* **15**(20), 12636–12653 (2007).
13. R. K. Wang, S. L. Jacques, Z. Ma, S. Hurst, S. R. Hanson, and A. Gruber, "Three dimensional optical angiography," *Opt. Express* **15**(7), 4083–4097 (2007).
14. A. Mariampillai, B. A. Standish, E. H. Moriyama, M. Khurana, N. R. Munce, M. K. K. Leung, J. Y. Jiang, A. E. Cable, B. C. Wilson, I. A. Vitkin, and V. X. D. Yang, "Speckle variance detection of microvasculature using swept-source optical coherence tomography," *Opt. Lett.* **33**(13), 1530–1532 (2008).
15. Y. K. Tao, A. M. Davis, and J. A. Izatt, "Single-pass volumetric bidirectional blood flow imaging spectral domain optical coherence tomography using a modified Hilbert transform," *Opt. Express* **16**(16), 12350–12361 (2008).
16. B. J. Vakoc, R. M. Lanning, J. A. Tyrrell, T. P. Padera, L. A. Bartlett, T. Stylianopoulos, L. L. Munn, G. J. Tearney, D. Fukumura, R. K. Jain, and B. E. Bouma, "Three-dimensional microscopy of the tumor microenvironment in vivo using optical frequency domain imaging," *Nat. Med.* **15**(10), 1219–1223 (2009).
17. E. M. Hillman, A. Devor, M. B. Bouchard, A. K. Dunn, G. W. Krauss, J. Skoch, B. J. Bacskaï, A. M. Dale, and D. A. Boas, "Depth-resolved optical imaging and microscopy of vascular compartment dynamics during somatosensory stimulation," *Neuroimage* **35**(1), 89–104 (2007).
18. A. Villringer, A. Them, U. Lindauer, K. Einhüpl, and U. Dirnagl, "Capillary perfusion of the rat brain cortex. An in vivo confocal microscopy study," *Circ. Res.* **75**(1), 55–62 (1994).
19. A. Devor, P. Tian, N. Nishimura, I. C. Teng, E. M. Hillman, S. N. Narayanan, I. Ulbert, D. A. Boas, D. Kleinfeld, and A. M. Dale, "Suppressed neuronal activity and concurrent arteriolar vasoconstriction may explain negative blood oxygenation level-dependent signal," *J. Neurosci.* **27**(16), 4452–4459 (2007).
20. H. Ren, T. Sun, D. J. MacDonald, M. J. Cobb, and X. Li, "Real-time in vivo blood-flow imaging by moving-scatterer-sensitive spectral-domain optical Doppler tomography," *Opt. Lett.* **31**(7), 927–929 (2006).
21. V. J. Srinivasan, S. Sakadžić, I. Gorczynska, S. Ruvinskaya, W. Wu, J. G. Fujimoto, and D. A. Boas, "Quantitative cerebral blood flow with optical coherence tomography," *Opt. Express* **18**(3), 2477–2494 (2010).
22. S. Yousefi, Z. Zhi, and R. K. Wang, "Eigendecomposition-based clutter filtering technique for optical micro-angiography," *IEEE Trans. Biomed. Eng.* **58**(8), 2316–2323 (2011).
23. R. Samatham, S. L. Jacques, and P. Campagnola, "Optical properties of mutant versus wild-type mouse skin measured by reflectance-mode confocal scanning laser microscopy (rCSLM)," *J. Biomed. Opt.* **13**(4), 041309 (2008).
24. R. A. Stepanoski, A. LaPorta, F. Raccuia-Behling, G. E. Blonder, R. E. Slusher, and D. Kleinfeld, "Noninvasive detection of changes in membrane potential in cultured neurons by light scattering," *Proc. Natl. Acad. Sci. U.S.A.* **88**(21), 9382–9386 (1991).
25. V. J. Srinivasan, S. Sakadžić, I. Gorczynska, S. Ruvinskaya, W. Wu, J. G. Fujimoto, and D. A. Boas, "Depth-resolved microscopy of cortical hemodynamics with optical coherence tomography," *Opt. Lett.* **34**(20), 3086–3088 (2009).
26. V. J. Srinivasan, J. Y. Jiang, M. A. Yaseen, H. Radhakrishnan, W. Wu, S. Barry, A. E. Cable, and D. A. Boas, "Rapid volumetric angiography of cortical microvasculature with optical coherence tomography," *Opt. Lett.* **35**(1), 43–45 (2010).
27. V. J. Srinivasan, D. N. Atochin, H. Radhakrishnan, J. Y. Jiang, S. Ruvinskaya, W. Wu, S. Barry, A. E. Cable, C. Ayata, P. L. Huang, and D. A. Boas, "Optical coherence tomography for the quantitative study of cerebrovascular physiology," *J. Cereb. Blood Flow Metab.* **31**(6), 1339–1345 (2011).
28. P. Cimalla, J. Walther, M. Mittasch, and E. Koch, "Shear flow-induced optical inhomogeneity of blood assessed in vivo and in vitro by spectral domain optical coherence tomography in the 1.3  $\mu\text{m}$  wavelength range," *J. Biomed. Opt.* **16**(11), 116020 (2011).
29. Y. Mutalifu, L. Holm, C. Ince, E. Theodorsson, and F. Sjöberg, "Multiple different laminar velocity profiles in separate veins in the microvascular network of brain cortex in rats," *Int. J. Clin. Exp. Med.* **4**(1), 10–16 (2011).
30. N. K. Logothetis, J. Pauls, M. Augath, T. Trinath, and A. Oeltermann, "Neurophysiological investigation of the basis of the fMRI signal," *Nature* **412**(6843), 150–157 (2001).
31. C. Iadecola, "Neurovascular regulation in the normal brain and in Alzheimer's disease," *Nat. Rev. Neurosci.* **5**(5), 347–360 (2004).
32. M. E. Raichle and M. A. Mintun, "Brain work and brain imaging," *Annu. Rev. Neurosci.* **29**(1), 449–476 (2006).
33. E. Hamel, "Cholinergic modulation of the cortical microvascular bed," *Prog. Brain Res.* **145**, 171–178 (2004).
34. B. Cauli, X. K. Tong, A. Rancillac, N. Serluca, B. Lambollez, J. Rossier, and E. Hamel, "Cortical GABA interneurons in neurovascular coupling: relays for subcortical vasoactive pathways," *J. Neurosci.* **24**(41), 8940–8949 (2004).
35. R. C. Koehler, D. Gebremedhin, and D. R. Harder, "Role of astrocytes in cerebrovascular regulation," *J. Appl. Physiol.* **100**(1), 307–317 (2006).
36. B. Stefanovic, E. Hutchinson, V. Yakovleva, V. Schram, J. T. Russell, L. Belluscio, A. P. Koretsky, and A. C. Silva, "Functional reactivity of cerebral capillaries," *J. Cereb. Blood Flow Metab.* **28**(5), 961–972 (2008).
37. V. J. Srinivasan, H. Radhakrishnan, E. H. Lo, E. T. Mandeville, J. Y. Jiang, S. Barry, and A. E. Cable, "OCT methods for capillary velocimetry," *Biomed. Opt. Express* **3**(3), 612–629 (2012).
38. P. J. Drew, A. Y. Shih, and D. Kleinfeld, "Fluctuating and sensory-induced vasodynamics in rodent cortex extend arteriole capacity," *Proc. Natl. Acad. Sci. U.S.A.* **108**(20), 8473–8478 (2011).

39. R. Fahraeus and T. Lindqvist, "The viscosity of the blood in narrow capillary tubes," *Am. J. Physiol.* **96**, 562–568 (1931).
  40. A. R. Pries, D. Neuhaus, and P. Gaehtgens, "Blood viscosity in tube flow: dependence on diameter and hematocrit," *Am. J. Physiol.* **263**(6 Pt 2), H1770–H1778 (1992).
  41. A. R. Pries, T. W. Secomb, and P. Gaehtgens, "Biophysical aspects of blood flow in the microvasculature," *Cardiovasc. Res.* **32**(4), 654–667 (1996).
  42. D. J. Faber and T. G. van Leeuwen, "Are quantitative attenuation measurements of blood by optical coherence tomography feasible?" *Opt. Lett.* **34**(9), 1435–1437 (2009).
  43. A. Grinvald, E. Lieke, R. D. Frostig, C. D. Gilbert, and T. N. Wiesel, "Functional architecture of cortex revealed by optical imaging of intrinsic signals," *Nature* **324**(6095), 361–364 (1986).
  44. I. Vanzetta, R. Hildesheim, and A. Grinvald, "Compartment-resolved imaging of activity-dependent dynamics of cortical blood volume and oximetry," *J. Neurosci.* **25**(9), 2233–2244 (2005).
- 

## 1. Introduction

The blood-oxygen-level-dependent functional magnetic resonance imaging (BOLD fMRI) signal [1,2] depends on the spatiotemporal interplay of oxygen consumption, blood flow, and blood volume [3]. Thus, precise understanding of this interplay between evoked metabolism and hemodynamics will improve understanding of this signal. A complete characterization of neurovascular coupling requires imaging of functional activation with both vascular compartment resolution and high temporal resolution. Optical imaging techniques such as optical intrinsic signal imaging (OISI) [4], diffuse optical imaging (DOI) [5,6], laser speckle imaging [7], laminar optical tomography [8] and two-photon microscopy [9] have enabled investigation of neurovascular coupling over a wide range of spatial and temporal scales. However, none of these techniques simultaneously achieves high spatial and temporal resolution, large field-of-view, and good depth penetration. Optical Coherence Tomography [10] is the optical analog of ultrasound, and critically, enables separation of changes in surface pial vasculature from the capillary-perfused tissue beneath. Angiographic methods, analogous to power Doppler ultrasound [11], have recently been developed for the visualization of blood vessels within scattering tissue. A number of OCT angiography techniques [12–16], which use dynamic red blood cell scattering as a contrast mechanism to detect vasculature, have been demonstrated. Phase variance, intensity variance, or complex signal variance maps of dynamic OCT signal, or "angiograms," are typically interpreted qualitatively as perfusion maps, wherein the source of contrast arises from a combination of motion and scattering, predominantly from moving red blood cells. While qualitative perfusion maps depict vascular anatomy, more powerful diagnostics could be achieved by relating imaging data directly to physiological parameters such as blood flow, blood volume, and red blood cell content.

Here, we use OCT angiography to investigate the hemodynamic response to functional activation in the rat somatosensory cortex, and propose dynamic backscattering as an indicator of dynamic red blood cell (dRBC) content. We show that, due to an increase in scattering, the attenuation coefficient increases during activation, potentially confounding depth-specific measurements. Consequently we propose a simple correction method to mitigate this potential confound, and determine depth specific dynamic backscattering changes. We show that arterial dRBC content increases along with prominent dilation, whereas venous dRBC content increases with slight dilation [17]. We also confirm that "all or none" capillary recruitment plays a negligible role in the hemodynamic response of the capillary bed, as indicated earlier by confocal microscopy [18].

## 2. Methods

Here, we first describe the OCT system and animal preparation, along with methods of somatosensory stimulation and response localization. We then present simple models to explain OCT dynamic and static signals in terms of attenuation and backscattering. Finally, we describe two complementary protocols for investigation of steady state and transient compartment-resolved hemodynamics with OCT angiography.

### 2.1 OCT system description

A 1310 nm spectral/Fourier domain OCT microscope was constructed for *in vivo* imaging of the rat cerebral cortex. The light source consisted of two superluminescent diodes combined using a 50/50 fiber coupler to yield a bandwidth of 150 nm. The axial (depth) resolution was 4.8  $\mu\text{m}$  in air (3.6  $\mu\text{m}$  in tissue). A spectrometer with a 1024 pixel InGaAs line scan camera operated at 47 kHz. Imaging was performed with a 10x objective, yielding a transverse resolution of 3.6 microns, or a 5x objective, yielding a transverse resolution of 7.2 microns.

### 2.2 Animal preparation

The animal procedures were approved by the Subcommittee on Research Animal Care at the Massachusetts General Hospital, where these experiments were performed. Male Sprague-Dawley rats (N = 5; 250-300 gms) were used in this study. The rats were initially anesthetized with 2-2.5% v/v isoflurane with a gas mixture of 80% air and 20% oxygen. Tracheostomy for mechanical ventilation and cannulation of the femoral artery for blood pressure monitoring and femoral vein for anesthetic administration were performed. Following catheterization, the animal was mounted on a stereotactic frame and a craniotomy was performed. Briefly, the scalp was retracted and a metal plate was attached to the exposed skull using bone screws. Using a dental burr, a  $\sim 5 \times 5 \text{ mm}^2$  skull region over the left forepaw region was thinned to translucency and then removed along with the dura. The exposed cortex was filled with 1.5% agarose (Sigma, MO USA), mixed in aCSF (pH 7.4; KCl 5mM, NaCl 125 mM, Glucose 10mM, CaCl<sub>2</sub> 3mM, and MgCl<sub>2</sub> 1mM, Sigma Aldrich, MO USA), and covered with a glass coverslip. Dental acrylic was used to seal the cranial window to the skull. To relieve excess intra-cerebral pressure, a ventriculostomy of the IVth ventricle was performed.

Following the surgical procedures, the anesthesia was changed to alpha-chloralose (loading dose – 40 mg/kg; maintaining dose – 50 mg/kg/hr). Throughout the surgical and imaging procedures, the blood pressure was monitored (SYS-BP1, WPI Inc., USA) via a transducer (BLPR2, WPI Inc., USA) connected to the arterial cannula and the animal's core temperature was maintained at 37 degrees Celsius using a heating blanket (Harvard Apparatus USA). Periodic measurement of blood gases ensured that the values of pO<sub>2</sub>, pCO<sub>2</sub> and pH were within physiological limits (pO<sub>2</sub> = 100 – 130 mmHg, pCO<sub>2</sub> = 32-40 mmHg, and pH = 7.35 – 7.45).

### 2.3 Stimulation

Two hypodermic needles were inserted into the plantar surface of the rat forepaw. The needles were connected by alligator clips to a stimulus isolator that delivered 300  $\mu\text{s}$  pulses at motor threshold ( $\sim 1$ -1.5 mA) when receiving computer controlled triggers. Electrical pulses were delivered at 3 Hz.

### 2.4 Response localization

Localization of the center of the neuronal response was performed before sealing the cranial window using a ball electrode [19]. The center of the neuronal response was determined by maximizing the measured electrical signal over a 3 x 3 grid spanning the cranial window. Two-dimensional optical intrinsic signal imaging (OISI) of the exposed cortex was then performed through the window by illuminating the cortex with a spectrally filtered Hg:Xe light source (570  $\pm$  5 nm). Two-dimensional images were acquired with a CCD camera during 25 second blocks with 2 second stimuli at 3 Hz. (Infinity 2-1M, Lumenera, CA). The CCD camera was connected by a USB cable to a computer, which saved the images. The images were later analyzed as a time series to determine the average response to a stimulus. While the map based on the peak fractional reflectance change was heavily weighted towards pial arteries where volume changes were the largest (Fig. 1A and Fig. 1B), the map based on the response temporal width yielded a more well-defined activation region (Fig. 1B and Fig. 1C) that agreed with the ball electrode data. The improved localization provided by the response temporal width is due to the fact that a faster return to baseline is typically observed

in the periphery as compared to the center of activation [19]. OCT imaging was always performed at the center of the OISI response, where the response width was maximal (Fig. 1D and Fig. 1E).

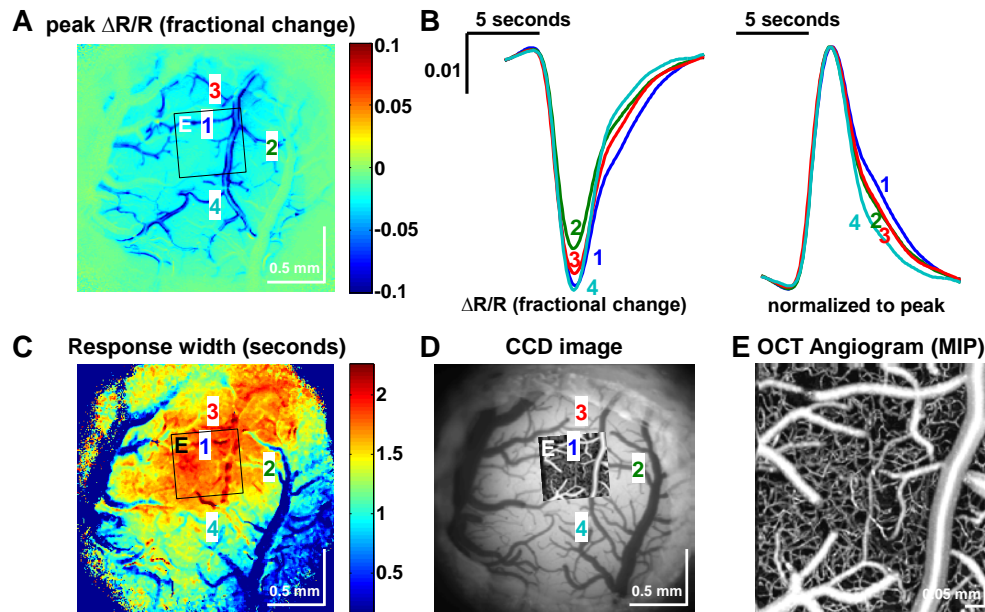


Fig. 1. OCT angiography location was chosen based on optical intrinsic signal imaging (OISI). (A) Peak fractional reflectance change ( $\Delta R/R$ ) map for OISI imaging at 570 nm, for a two second stimulus. The map is heavily weighed to the pial arteries, where the blood volume changes and relative reflectance changes are highest. (B) Time courses for fractional reflectance changes at locations labeled 1-4 (left). When normalized curves are plotted, differences in the response widths are evident (right). (C) Spatial map of the response width, showing better response localization than (A). (D) Single image at 570 nm, with OCT maximum intensity projection (MIP) angiogram overlay. (E) OCT MIP angiogram showing volumetric region measured during activation.

### 2.5 Model of static and dynamic scattering

Previously, it was proposed that a complex OCT image can be considered as a superposition of fields from multiple scatterers [15,20]. Neglecting noise, the complex OCT signal can be described as the superposition of a static signal component and a dynamic signal component [21,22] within a single voxel. The temporal properties of the signal from a given voxel are characterized by the autocorrelation function. Moreover, one may distinguish between flow decorrelation time scales ( $<20$  milliseconds) and hemodynamic changes time scales ( $>100$  milliseconds), by analysis of time courses with a sliding window. We use the variables  $\tau$  and  $T$  to designate the fast and slow time scales, respectively. Each term in the autocorrelation function can be associated with a specific component of the complex OCT signal. The autocorrelation can be represented as shown below:

$$R(x,y,z,\tau,T)=R_s(x,y,z,\tau,T)+R_d(x,y,z,\tau,T) \quad (1)$$

The static signal power ( $I_s$ ) and dynamic signal power ( $I_d$ ) are defined by evaluating the corresponding terms in the autocorrelation at a time lag  $\tau = 0$ .

$$I_s(x,y,z,T)=R_s(x,y,z,0,T) \quad (2)$$

$$I_d(x,y,z,T)=R_d(x,y,z,0,T) \quad (3)$$

## 2.6 Model of signal attenuation and correction procedure

Here, we outline and justify methods for quantifying changes in dynamic red blood cell (dRBC) content. Briefly, our method involves removal of static signal, estimation of dynamic signal power, and finally, normalization of dynamic signal power to the static signal power from nearby non-vascular tissue to determine relative changes in dynamic backscattering.

First, we present models of static and dynamic scattering to further describe the signals described above. We assume a simple single scattering model with an attenuation coefficient that includes the effects of scattering and absorption.

$$\mu_t = \mu_s + \mu_a \quad (4)$$

The scattering coefficient  $\mu_s$  can be taken to comprise both scattering from static brain tissue and moving blood cells, whereas the absorption coefficient  $\mu_a$  is mainly due to water at 1300 nm. (A more accurate version of Eq. (4) can be obtained by replacing  $\mu_s$  with  $\mu_s a(g)$  [23], where  $a(g)$  accounts for detection of multiply forward scattered light). Secondly, we assume that the detected OCT signal can be divided into a static signal,  $I_s$  (Eq. (2)), and a dynamic signal,  $I_d$  (Eq. (3)). If only single scattered light is detected, the static and dynamic signals are distinguished by whether the single backscattering event occurs from a stationary or moving particle. A simple single scattering model therefore describes the depth dependence of the static signal:

$$I_s(x, y, z, T) = B_s(x, y, z) h_{\text{spectrometer}}(z) h_{\text{confocal}}(z) \exp[-2\mu_t(x, y, T)z] \quad (5)$$

The dynamic signal can be described similarly:

$$I_d(x, y, z, T) = B_d(x, y, z) h_{\text{spectrometer}}(z) h_{\text{confocal}}(z) \exp[-2\mu_t(x, y, T)z] \quad (6)$$

In the above expressions,  $h_{\text{confocal}}$  and  $h_{\text{spectrometer}}$  are functions of path length  $z$  that account for the confocal gate and spectrometer sensitivity roll-off, respectively. The static and dynamic backscattering are given by  $B_s$  and  $B_d$ , respectively.

### 2.6.1 Dynamic backscattering and dynamic RBC content

Two important changes occur in Eq. (5) and Eq. (6) during activation. Firstly, the dynamic backscattering ( $B_d$ ) increases, due to an increase in red blood cell density and velocity. Secondly, the attenuation coefficient ( $\mu_t$ ) increases due to increased attenuation from scattering. As  $\mu_t z$  appears in the exponent of Eq. (5) and Eq. (6), an increase in  $\mu_t$  has a greater influence on signal levels at greater depths. The static backscattering ( $B_s$ ) is assumed not to change. Approximately constant static backscattering was confirmed by performing measurements of signal intensity in avascular regions near the cortical surface. We note here that fast-optical signals, while they would constitute changes in static scattering, are at least two orders of magnitude smaller than the observed slow hemodynamic scattering changes [24], and therefore are not considered here. The assumption that static backscattering remains constant over time may not be valid under pathological conditions such as cortical spreading depression or severe ischemia.

The attenuation coefficient  $\mu_t$  is known to increase due to increased scattering during functional activation [25], resulting in reduced signals from greater tissue depths. The most likely mechanism for the rise in  $\mu_t$  is an increase in red blood cell number during activation. Red blood cell orientation changes, astrocyte swelling, and tissue compression resulting from increased blood volume are other possible mechanisms. Critically, both static and dynamic signals were assumed to experience the same attenuation coefficient. If static backscattering does not change, the static signal conveniently serves as a “reference.” Thus, it is possible to normalize the dynamic signal to the static signal acquired at the same time and depth to remove the confounding effects of attenuation coefficient changes, as shown below.

$$I_{\text{norm}}(x,y,z,T) = \frac{I_d(x,y,z,T)}{I_s(x,y,z,T)} = \frac{B_d(x,y,z,T)}{B_s(x,y,z)} \quad (7)$$

The normalized signal  $I_{\text{norm}}$  in Eq. (7) gives the ratio of dynamic to static backscattering. In practice  $I_s$  is averaged over a local region, devoid of vessels, to reduce speckle noise. The relative normalized signal,  $\Delta I_{\text{norm}}/I_{\text{norm}}$ , can then be defined as follows:

$$\frac{\Delta I_{\text{norm}}(x,y,z,T)}{I_{\text{norm}}(x,y,z,0)} = \frac{I_{\text{norm}}(x,y,z,T) - I_{\text{norm}}(x,y,z,0)}{I_{\text{norm}}(x,y,z,0)} \quad (8)$$

Combining Eq. (7) with Eq. (8), we obtain the following:

$$\frac{\Delta I_{\text{norm}}(x,y,z,T)}{I_{\text{norm}}(x,y,z,0)} = \frac{B_d(x,y,z,T) - B_d(x,y,z,0)}{B_d(x,y,z,0)} \quad (9)$$

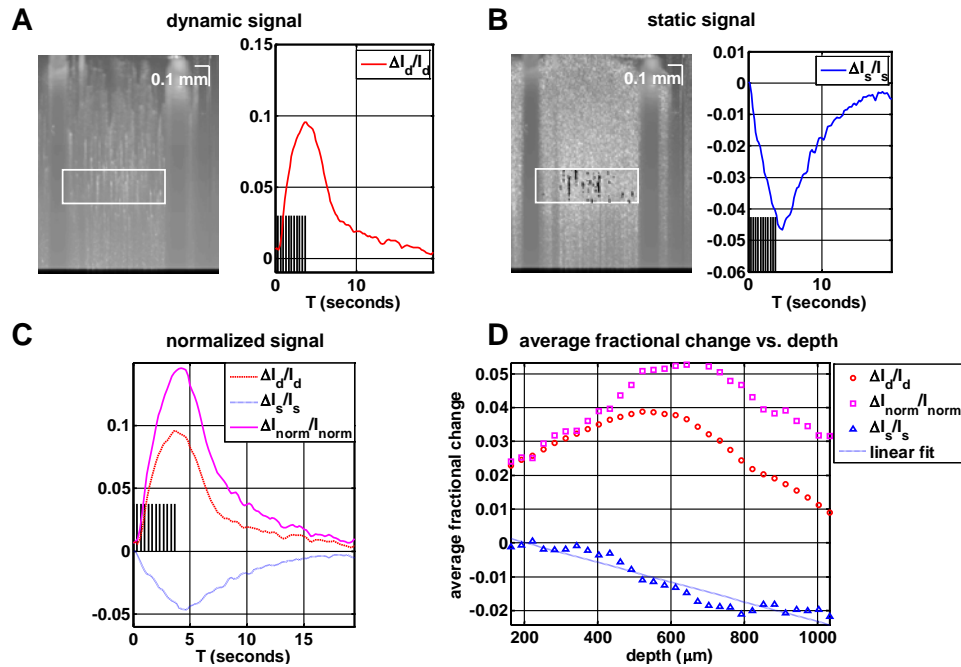


Fig. 2. A correction procedure was applied to determine depth-specific dynamic backscattering changes. (A) The OCT angiogram, representing the dynamic signal  $I_d$ , with relative changes in a region of interest (white rectangle) plotted during stimulation (average of 12 trials). (B) Raw OCT intensity image, with relative changes of static signal in the same region of interest plotted during stimulation. The static signal decrease is due to a  $\mu_i$  increase (Eq. (5)), which likewise affects the dynamic signal (Eq. (6)). (C) As a solution to this confound, relative changes in normalized signal (magenta) are determined from the ratio of dynamic to static signal within the same region of interest. (D) Plot of the average fractional change in normalized signal (magenta squares) indicates a maximum at a cortical depth of between 500 and 700 microns. The average fractional change in static signal exhibits a linear dependence vs. depth (blue triangles), supporting the assumption of an increase in the attenuation coefficient. To achieve a larger depth of focus and investigate laminar differences, a 7.2 micron transverse resolution was used for this figure.

Hence, under the aforementioned assumptions, the quantity in Eq. (9) is a depth-specific measure of hemodynamics. While there are other scattering components in blood, RBCs are the most numerous intravascular scatterers; hence dynamic backscattering changes are an indicator of changes in dRBC content that accompany activation. The critical assumptions in

arriving at this interpretation are that 1) static backscattering does not change and that 2) both static and dynamic signals experience the same attenuation with depth due to scattering.

Figure 2A shows the dynamic signal image ( $I_d$ , log scale), with relative changes in a region of interest (white rectangle) plotted. The dynamic signal, averaged over the region of interest, increases during activation. However, the quantitative interpretation of this increase is confounded by the above-mentioned increase in  $\mu_t$ . Figure 2B shows the OCT intensity image ( $I_s$ , log scale), along with the mask used to exclude dynamic signal in black. The static signal during activation is reduced (Fig. 2B), due to an increase in  $\mu_t$  (Eq. (5)). Therefore, dynamic signal was normalized to static signal to correct for the change in  $\mu_t$  (Eqs. (7)-(9)), and relative changes were plotted in Fig. 2C. When the normalized time courses are plotted, laminar differences in response magnitude are evident, apparently showing that the largest dynamic backscattering changes occur between 500 and 700 microns cortical depth (Fig. 2D). The mean  $\Delta\mu_t$  for a 4 second 3 Hz stimulus, averaged over the 20 period after stimulus onset, was  $0.014 \pm 0.003 \text{ mm}^{-1}$  ( $N = 4$ ).

### 2.7 Angiography protocols

Two imaging protocols were used: i) continuous stimulation at 3 Hz with steady-state three-dimensional scanning at baseline and during activation (Fig. 3A) and ii) asynchronous block stimulus and repeated three-dimensional scanning (Fig. 3B). For both protocols, a 3.6 micron transverse resolution was used, the focus was placed 100-200 microns below the cortical surface, and data was analyzed up to a cortical depth of 400 microns.

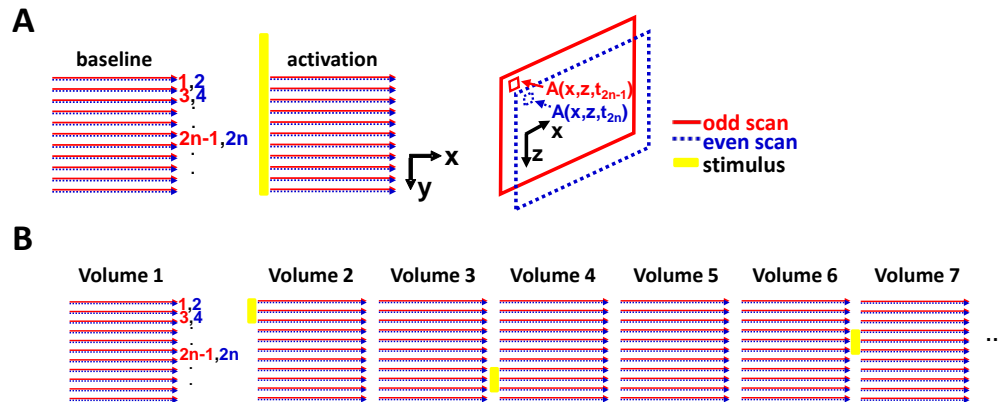


Fig. 3. OCT angiography scanning protocols. (A) Three-dimensional scanning protocol used to determine compartment-resolved steady-state changes during a long stimulus ( $>10$  s). (B) Four-dimensional asynchronous scanning protocol used to determine time-courses of compartment-resolved changes during a short (2 s) stimulus.

#### 2.7.1 3-D angiography

Figure 3A shows a three-dimensional scanning protocol for volumetric angiography that samples the same transverse location twice per volume. OCT angiograms were acquired by repeating a volumetric scanning protocol that sampled each spatial location twice [26]. A total of 1024 images at 512 y locations were acquired in 12 s to generate a single volumetric angiogram of  $1.25 \text{ mm} \times 1.25 \text{ mm}$ . At 512 axial scans per image, each location was sampled at 11 ms intervals. A first volume was acquired, then stimulation was performed for 10 seconds without data acquisition, and stimulation continued uninterrupted during acquisition of the second volume.

#### 2.7.2 4-D angiography

Figure 3B shows a four-dimensional scanning protocol with asynchronous, or staggered, stimulation and data acquisition, used to investigate time courses of compartment-resolved

changes. The central goal of this protocol was to simultaneously achieve a large field-of-view and high temporal resolution. At 256 axial scans per image, each location was sampled at 7 ms intervals. A total of 512 images at 256 y locations were acquired in 3.6 seconds to generate a single volumetric angiogram of 0.63 mm x 0.63 mm. A 2 second stimulus with an inter-stimulus interval of 23 seconds (block period of 25 seconds) was used. 10 blocks were presented per run. Three computers were involved in these experiments; 1) a stimulus computer generating stimulus trains at a period of  $t_{\text{rep}} = 25$  seconds controlling an amplifier and linear stimulator, an OCT computer that acquired camera line triggers and generated frame triggers and galvanometer signals for acquisition control, and a third computer that acquired both the stimulus triggers and the frame triggers. For the purposes of this discussion, we assume that the time between consecutive B-scans  $\Delta t = t_{2n} - t_{2n-1}$  is small. Angiograms were generated by taking the absolute value of the complex difference between consecutive frames:

$$\Delta A(x,z,t) = \Delta A\left[x,z,\frac{(t_{2n}+t_{2n-1})}{2}\right] = \frac{|A(x,z,t_{2n}) - A(x,z,t_{2n-1})|}{\sqrt{2}} \quad (10)$$

In the above expression,  $t$  is given by  $(t_{2n} + t_{2n-1})/2$ . If the time interval  $\Delta t = t_{2n} - t_{2n-1}$  between consecutive frames is much greater than the decorrelation time, the angiogram amplitude is insensitive to velocity changes. However, if the time interval is on the order of the decorrelation time, the amplitude will be affected by both velocity changes and changes in RBC content. The complex subtraction of Eq. (10) can be explained as a digital filtering procedure, shown in Fig. 4, which removes static scattering, or “clutter” [15].

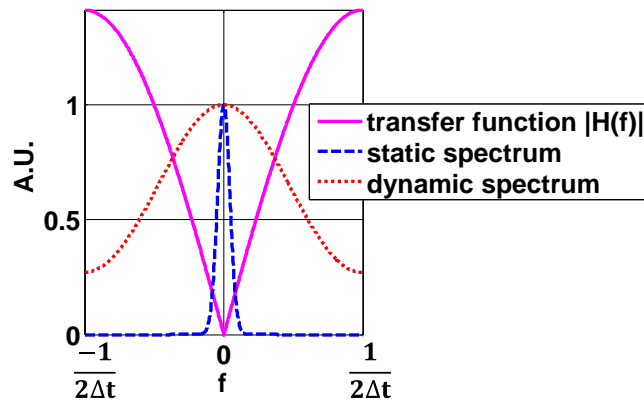


Fig. 4. Separation of static and dynamic signal can be interpreted as a high-pass filtering procedure. A change in the dynamic spectrum width (related to velocity) or area (related to red blood cell number or orientation) may affect the measured dynamic signal in Eq. (10) and Eq. (11).

By asynchronously running a block stimulus paradigm such that the least common multiple of the inter-stimulus interval  $t_{\text{rep}}$  and the volumetric repetition time  $t_{\text{vol}}$  was greater than the time for one run (set of trials), a given spatial location was sampled at a different time with respect to the stimulus, for each repeated volume. The frame triggers and the stimulus triggers were recorded, thus the y location of the angiogram as well as the temporal location with respect to the stimulus could be determined. Therefore it was possible to determine the exact location of each angiogram pixel in space and in time relative to the last stimulus. A four-dimensional volume of functional activation,  $I_d(x,y,z,T)$  could thus be constructed as shown below:

$$I_d[x,y,z,T] = I_d[x,v_y \times \text{mod}(t-t_{0,\text{vol}},t_{\text{vol}}),z,\text{mod}(t-t_{0,\text{stim}},t_{\text{rep}})] = \Delta A(x,z,t)^2 \quad (11)$$

In the above expression,  $v_y$  is the velocity of  $y$  scanning. The acquisition for repeated volumes begins at  $t_{0,vol}$ , while the first stimulus begins at  $t_{0,stim}$ . Due to the asynchronous scanning protocol, each location is not sampled at uniform time intervals with respect to the stimulus. Thus it was necessary to interpolate and resample this data at evenly spaced times before displaying movies. The interpolation procedure is valid if dynamics are repeatable on successive stimulus trials. Similar scanning protocols are used frequently in fMRI experiments where multiple slices are acquired asynchronously with respect to the stimulus.

### 3. Results

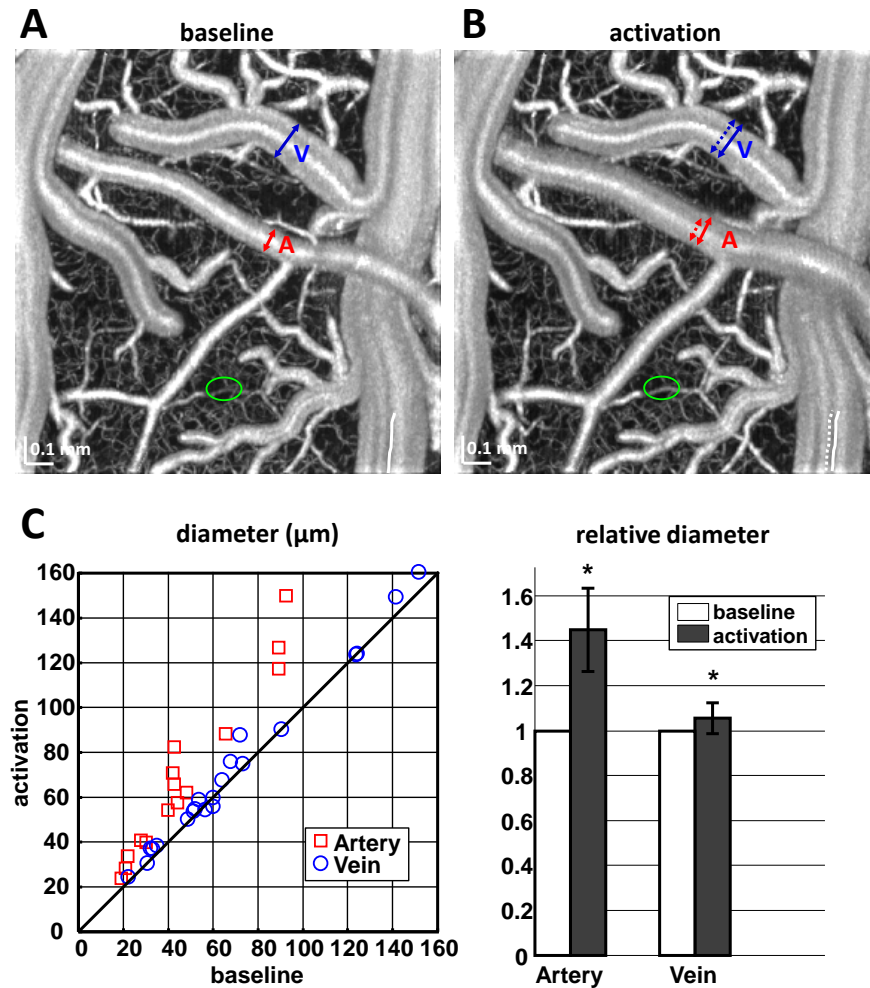


Fig. 5. Three-dimensional volumetric imaging during continuous 3 Hz stimulation shows salient arterial dilation, subtle venous dilation, and apparent lack of capillary recruitment. Comparison of baseline (A) and activation (B) MIP angiograms shows that only one vessel branch which was not perfused at baseline becomes perfused during activation (green circle). Moreover, as depicted in the OCT angiograms, arteries clearly dilate (red arrows), while venous changes are more subtle (blue arrows). A change in the “striped” scattering pattern caused by RBC orientation in the surface vein is evident during activation (white lines, dotted represents baseline). This is due to higher flow in venules draining the activated region, and the presence of non-mixing flow streams. (C) Comparison of vessel diameters at baseline and during activation shows that while both arteries and veins dilate, arterial dilation is considerably greater than venous dilation.

Three-dimensional angiography (Fig. 3A) at baseline and during activation shows very little evidence of capillary recruitment (Fig. 5A and Fig. 5B). This finding is consistent with the two-photon microscopy and OCT angiography overlay performed previously [27], which showed that the vast majority of vessels perfused with plasma are also perfused with RBCs. Only one vessel branch which was not RBC perfused at baseline become perfused during activation (green circle in Fig. 5B). Moreover, arteries dilated (red arrows in Fig. 5B, dotted arrows represent baseline), while veins barely dilated (blue arrows in Fig. 5B, dotted arrows represent baseline). The different relative dilations of arteries (CI = 13.7-29.7 micron difference, 34.6%-55.2%) and veins (CI = 1.2-5.2 micron difference, 2.4%-8.7%) are shown in Fig. 5C. During activation, a change in the “striped” scattering pattern caused by RBC orientation [28] in the surface vein is evident (white lines in Fig. 5B, dotted represents baseline). This is due to a shift in the distribution of flows among draining venules that causes a change in the pattern of non-mixing flow streams in the draining vein [29].

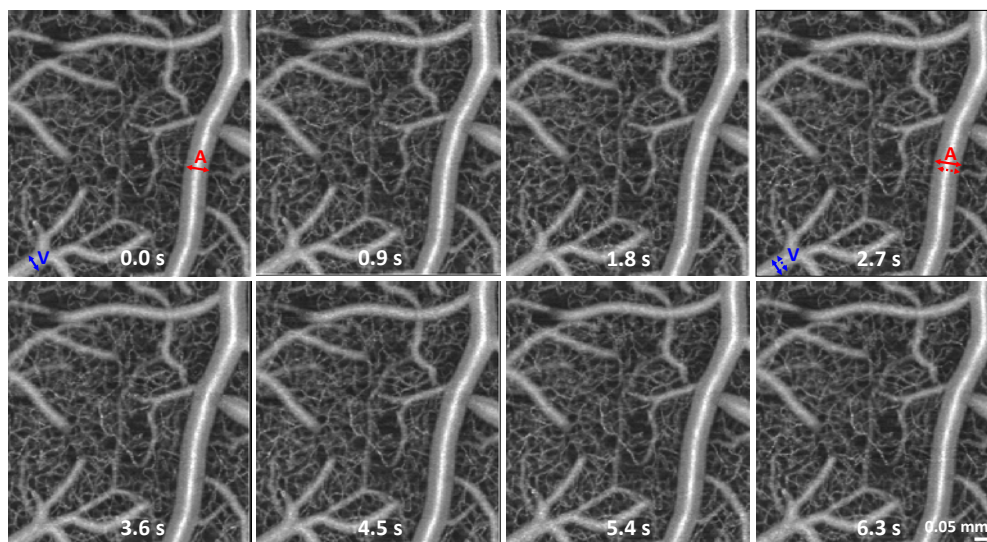


Fig. 6. Frames from a four-dimensional (4-D) movie of the hemodynamic response to functional activation, obtained from resampling a series of 3-D data sets obtained by the protocol shown in Fig. 4B. A maximum intensity projection over each resampled three-dimensional data set was performed to generate *en face* images at each time point relative to the stimulus. The stimulus is from 0 to 2 seconds. At 2.7 seconds, clear arterial dilation relative to baseline is observed (Media 1).

A three-dimensional angiographic movie (Fig. 6) created using the protocol shown in Fig. 3B confirms prominent arterial dilation, subtle venous dilation, and a lack of capillary recruitment during activation (see Media 1). The stimulus is from 0 to 2 seconds, and diameters are marked at 2.8 s (dotted corresponds to baseline). Figure 7 shows interpolated angiographic images of compartment-resolved responses at baseline and during maximal activation (2-4 seconds after stimulus onset) using the 4-D angiography protocol (Fig. 3B). A maximum intensity projection over each resampled three-dimensional data set was performed. Baseline images (Fig. 7A) were averaged between 23 and 25 seconds after the stimulus onset, while peak activation images (Fig. 7B) were averaged between 2 and 4 seconds after the stimulus onset. At peak activation (Fig. 7E), arteries dilated (CI = 2.1-4.7 micron difference, 6.5%-13.9% normalized difference), while veins barely dilated (CI = 0.2-1.5 micron difference, 0.0%-4.1% normalized difference) (see Media 2). In general, prominent dilation of arterioles and arteries, and slight dilation of veins and venules was observed. Capillary dilation was not quantitatively evaluated; however capillary width was qualitatively unchanged, indicating that motion artifacts are insignificant. We rarely observed a capillary which was unperfused or “underperfused” with RBCs become perfused under

activation. A notable exception is circled in green. Also, the highly scattering “stripe” in the draining pial vein moves during activation (Fig. 7B, dotted line represents baseline). This is due to an increase in the flow from the venules draining the activated region, which changes the pattern of non-mixing flow streams.

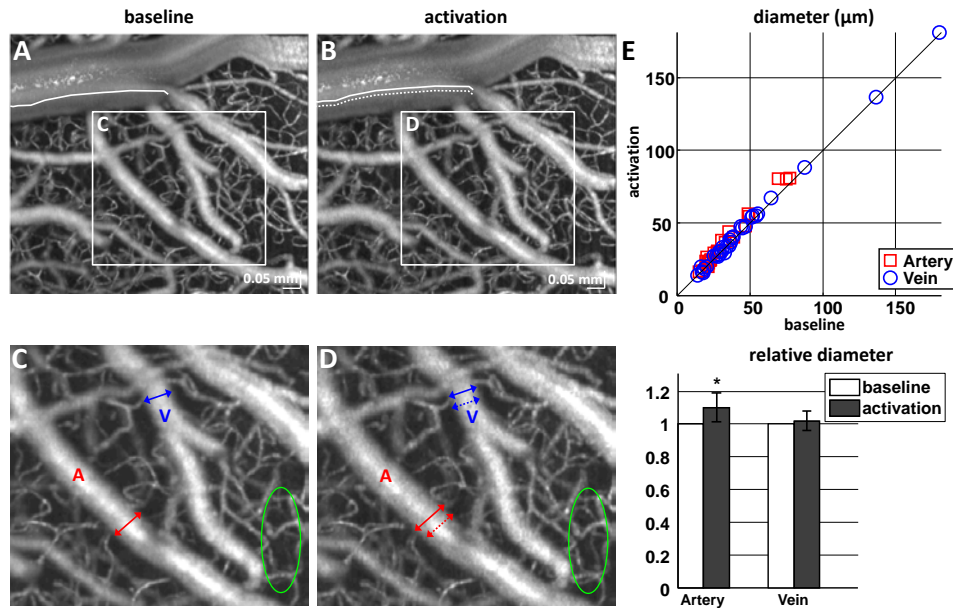


Fig. 7. Compartment resolved changes in dRBC content were investigated with a 4-D scanning protocol at baseline (23-25 s after stimulus onset) and during maximal activation (2-4 s after stimulus onset). (A-B) The highly scattering stripe corresponding to non-mixing flow streams moves during activation (dotted white line in B corresponds to baseline). (C-D) In agreement with Fig. 5, arteries dilate, while veins barely dilate, and capillary recruitment is absent save one exception (green circle). (E) Relative diameter changes in arteries, but not veins, are statistically significant (N = 3) (Media 2).

Compartment-resolved changes in dynamic backscattering (Eq. (9)) were also investigated (Fig. 8). Individual regions of interest were selected, and relative signal changes were investigated in these regions. Regions of interest were selected to encompass relevant vessels at peak dilation. Increases in the dynamic backscattering were observed in arterial (Fig. 8A), arteriolar (Fig. 8B), capillary (Fig. 8C), and venular compartments (Fig. 8D). The average of all ROIs is shown as a solid black curve in each plot. Across 4 animals, the peak increase in dynamic backscattering was largest in the arterial/arteriolar compartment (CI = 12.4-15.8%), and smaller in the capillary compartment (CI = 5.8-12.4%) and the venular/venous compartment (CI = 2.8-5.6%).

#### 4. Discussion

In spite of many years of research, controversy still exists about the origins of the cortical hemodynamic response during functional activation and its neuronal underpinnings [30–32]. Elegant studies have attempted to elucidate the spatiotemporal evolution of the hemodynamic response [17] as well as the chemical messengers and cell types behind it [33–35]. A basic understanding of these mechanisms requires imaging of the hemodynamic response with high spatiotemporal resolution. Here, we investigate scattering-based methods of imaging the cortical hemodynamic response to functional activation using OCT angiography. These methods enable more detailed and comprehensive characterization of the neurovascular relationship across compartments than was previously possible.

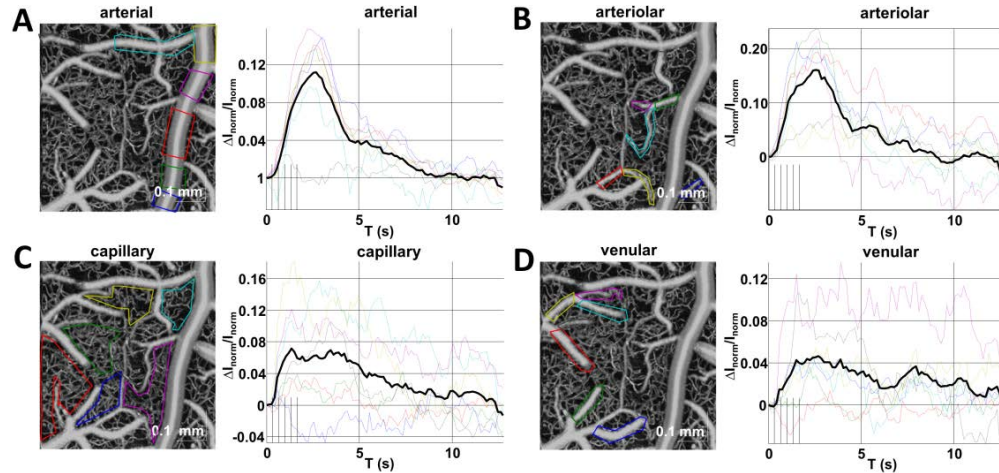


Fig. 8. Compartment-resolved changes in the normalized dynamic signal, reflecting dRBC content changes, were investigated. We selected individual regions of interest in the OCT angiograms, and investigated relative signal changes in these regions. (A-B) Large increases in the dynamic backscattering signal in both the arterial and arteriolar compartments were observed. (C-D) Modest increases in the dynamic backscattering signal in both the venular and capillary compartments were observed, with delayed returns to baseline. The average of all ROIs is shown as a solid black curve.

#### 4.1 Capillary recruitment does not occur to a significant degree

Our data (Fig. 5A-B and Fig. 7C-D) suggests that “all or none” capillary recruitment is insufficient to explain the changes in the capillary bed [18], at least up to the cortical depths measured in this study (400 microns). Consistent with this observation, we observe dRBC content increases in capillaries (Fig. 8C). This suggests that changes in flow and oxygen delivery are more likely to be explained through ensemble changes in capillary linear hematocrits and velocities. An interesting future question is how heterogeneities of capillary velocities and hematocrits change after activation [36]. While our group recently developed OCT correlates of capillary velocity [37], we strongly caution that these correlates require careful and systematic validation; therefore, we have not explicitly investigated heterogeneities in capillary perfusion here.

#### 4.2 There is evidence of prominent arterial dilation and subtle venous dilation

Our data show that arteriolar/arterial dilation is conspicuous during activation (Fig. 5, Fig. 6, and Fig. 7) while venular/venous dilation is subtle if present. Our finding of detectable vein dilation during a long stimulus (Fig. 5), but not a short stimulus (Fig. 7), is consistent with a recent study in awake mice [38]. However, subtle changes in vessel diameter depicted by OCT angiography must be interpreted with caution. Vessel diameters are classically defined by the plasma width, or distance between the inner edges of the vessel wall. In this study, diameters were determined from the region of dynamic scattering blood contents. One possible confound is therefore the Fahraeus-Lindqvist effect [39–41]. Due to this effect, erythrocytes preferentially locate near the center of the vessel, leaving a plasma only, or “cell-free,” layer near the vessel wall. Thus, the vessel diameter measured using blood cell scattering does not correspond to the true diameter of the vessel. In principle, a flow increase in the absence of a vessel diameter change would cause an increase in the plasma cell-free layer, and thus a decrease in the apparent diameter measured using our method. Another possible confounding effect is that the dynamic signal increases after activation, which alone may increase the apparent vessel thickness as the signal at the edges of the vessel surpasses the background noise level. For this reason, we measured vessel diameters at only two time

points using averaged data at baseline and during maximal activation to improve the signal to noise ratio.

#### 4.3 Interpretation of dynamic backscattering changes

In this work, we interpret dynamic backscattering as indicating changes in dRBC content. However, the dynamic signal may be affected by changes in RBC speed or orientation in addition to density. As our technique for isolating the dynamic signal uses a high-pass filter, an increase in RBC speed could conceivably add frequency content above the cutoff frequency, via either increased Doppler shift or decorrelation rate (frequency broadening, see Fig. 4). However, a close examination of our data argues against this possibility. In veins, red blood cell speed tends to return to baseline more rapidly and occasionally undershoot, similar to velocity [25]. The delayed return to baseline of the dynamic backscattering in venules suggests a “volume-like” and not a “flow-like” response (Fig. 8C and Fig. 8D). Thus, the dynamic backscattering kinetics resemble RBC content rather than velocity. In support of this observation, we observed similar delayed scattering increases in pial veins in the raw OCT images, *without* the use of a high-pass filter, suggesting that the high-pass filter does not play a critical role in the observation of a response. Taken together, our data suggest that the dynamic backscattering increase in Fig. 8 is predominantly due to an increase in RBC density. One last potential confound is that RBC orientation changes may result in scattering changes due to the high scattering anisotropy of RBCs. We cannot eliminate orientation changes as a possible factor contributing to the evoked changes in dynamic backscattering; however, it seems unlikely that a consistent directional scattering change could persist after averaging over vessels of many sizes and orientations.

It should be noted that while our data show evidence of an increase in venular hematocrit, quantification of the relative change in hematocrit from the scattering changes requires knowledge of the baseline hematocrit, as the relationship is nonlinear [42]. Nevertheless, our data support the assertion that both capillary and venous red blood cell content increase during functional activation.

#### 4.4 Scattering-based investigation of hemodynamics

In this work, we demonstrate that optical scattering signals, rather than absorption changes, can be used to investigate cortical hemodynamic responses. This represents a novel and complementary approach when compared to conventional optical intrinsic signal imaging [43]. Here, we interrogate dRBC content changes during functional activation, rather than hemoglobin changes that are conventionally probed. Imaging is performed at infrared wavelengths where differences between oxy- and deoxy-hemoglobin absorption are negligible; hence saturation effects are not expected to play a role in the observed signals. Thus, our approach provides pure hemodynamic responses, without possible confounds from oximetric changes [44]. Our observation that the hemodynamic response is largest in arteries agrees with earlier studies based on hemoglobin absorption [44].

### 5. Conclusion

Scattering-based techniques for characterizing dRBC content and diameter responses across vascular compartments during functional activation were demonstrated in the rat somatosensory cortex. All compartments responded to activation with increases in dRBC content, with subtle diameter changes in veins [17] and prominent diameter changes in arteries. “All or none” capillary recruitment did not occur to a significant degree during activation, up to the cortical depths measured in this study.

### Acknowledgments

We acknowledge support from the National Institutes of Health (R00NS067050, EB00790, and EB001954 R01), the American Heart Association (11IRG5440002), and the Glaucoma Research Foundation Catalyst for a Cure 2. We thank Weicheng Wu for the rat surgery and Bruce Rosen and Maria Angela Franceschini for general support.